



# Modulation of charge carrier dynamics of $\text{Na}_x\text{H}_{2-x}\text{Ti}_3\text{O}_7\text{-Au-Cu}_2\text{O}$ Z-scheme nanoheterostructures through size effect



Ying-Chih Pu, Wei-Hao Lin, Yung-Jung Hsu\*

Department of Materials Science and Engineering, National Chiao Tung University, Hsinchu, Taiwan 30010, Republic of China

## ARTICLE INFO

### Article history:

Received 28 April 2014

Received in revised form 30 June 2014

Accepted 7 August 2014

Available online 17 August 2014

### Keywords:

Charge transfer

Semiconductors

Composites

Photocatalysis

Structure-property relationships

## ABSTRACT

For the first time we presented the interfacial charge carrier dynamics for three-component semiconductor-metal-semiconductor Z-scheme nanoheterostructure system. The samples were prepared by selectively depositing a thin layer of  $\text{Cu}_2\text{O}$  on the Au surface of Au nanoparticle-decorated  $\text{Na}_x\text{H}_{2-x}\text{Ti}_3\text{O}_7$  nanobelts (denoted as ST-Au NBs) using the photodeposition method. For ST-Au- $\text{Cu}_2\text{O}$  NB heterostructures, the embedded Au may act as carrier-transfer mediator to promote the electron transfer from the conduction band of ST to the valence band of  $\text{Cu}_2\text{O}$ . This vectorial charge transfer would give rise to electron accumulation at  $\text{Cu}_2\text{O}$  and hole concentration at ST, which achieved superior charge carrier separation over the two-component counterparts of ST-Au and ST- $\text{Cu}_2\text{O}$ . The quantum size effect was significant in the deposited  $\text{Cu}_2\text{O}$ , which was exploited to tune the band structure of  $\text{Cu}_2\text{O}$ , modulate the charge carrier dynamics of ST-Au- $\text{Cu}_2\text{O}$  NBs, and thereby enhance the resultant photocatalytic performance. Time-resolved photoluminescence spectra were measured to quantitatively analyze the electron transfer event between ST and Au for ST-Au- $\text{Cu}_2\text{O}$  NBs, which was found dependent on the  $\text{Cu}_2\text{O}$  shell thickness. As the  $\text{Cu}_2\text{O}$  thickness decreased, ST-Au- $\text{Cu}_2\text{O}$  NBs showed an increased electron-scavenging rate constant due to the increased driving force of electron transfer. The carrier dynamics results were fundamentally consistent with those of the performance evaluation in photocatalysis, in which ST-Au- $\text{Cu}_2\text{O}$  NBs exhibited enhanced photocatalytic efficiency as the  $\text{Cu}_2\text{O}$  thickness decreased. Systematic understanding of the interfacial charge dynamics of Z-scheme mechanism shall pave the way for the realization of artificial photosynthesis by using heterogeneous photocatalysts, where the effectiveness of charge separation and the merit of high redox powers are determinant.

© 2014 Elsevier B.V. All rights reserved.

## 1. Introduction

As inspired by the natural photosynthesis in green plants, “Z-scheme” charge transfer system has been intensively studied because it allows capture of a large part of the solar spectrum for solar fuel production [1–3]. In particular, spatial separation of the reduction and oxidation centers is attainable in such a two-step photoexcitation system, which can minimize the undesirable back-reaction to enhance the overall photoconversion efficiency [4,5]. Recently, all-solid-state three-component semiconductor-metal-semiconductor nanoheterostructures with Z-scheme mechanism have demonstrated much higher photocatalytic activity than the single- and two-component counterpart systems. For

semiconductor-metal-semiconductor Z-scheme nanoheterostructures, the embedded metal may act as carrier-transfer mediator to promote a vectorial charge transfer pathway, which increases the oxidizing and reducing powers for photocatalysis. Till now, miscellaneous kinds of semiconductor nanoheterostructures with Z-scheme band structure have been proposed and fabricated [6–19]. For example,  $\text{CdS-Au-TiO}_2$  Z-scheme nanojunction showed much higher photocatalytic activity than individual constituents and binary counterparts toward the reduction of methyl viologen [6]. Besides, Z-scheme  $\text{AgCl-Ag-TaON}$  was successfully prepared, which exhibited superior photocatalytic performance in the degradation of organic dyes [7]. Moreover, C-doped  $\text{TiO}_2$  was combined with Au and CdS to achieve a visible-light-responsive Z-scheme mechanism which demonstrated superb photocatalytic  $\text{H}_2$  generation [8]. These developments have witnessed a rising demand for the realization of Z-scheme mechanism to further the advancement of photoconversion technology.

\* Corresponding author. Tel.: +886 3 5712121x55317; fax: +886 3 5724724.  
E-mail addresses: [yhsu@cc.nctu.edu.tw](mailto:yhsu@cc.nctu.edu.tw), [yhsu@mail.nctu.edu.tw](mailto:yhsu@mail.nctu.edu.tw) (Y.-J. Hsu).

Modulation of charge carrier dynamics is important to the development of light-energy conversion system that utilizes semiconductor nanoheterostructures [20–25]. In Yang's study, the interfacial charge dynamics of Au-CdS core-shell nanocrystals have been investigated with time-resolved photoluminescence (PL) spectroscopy. By probing the PL lifetime of CdS, the electron transfer rate constant from CdS shell to Au core can be quantitatively analyzed, which was in good accordance with the results of photocatalytic activity evaluation [23]. On the other hand, the high correlation between photoconversion efficiency and interfacial charge dynamics was revealed in CdSnO<sub>3</sub>-decorated CdS nanowires, which is a representative example of semiconductor-semiconductor nanoheterostructures [24]. Furthermore, three-component In<sub>2</sub>O<sub>3</sub>-TiO<sub>2</sub>-Pt heterojunction system was also investigated and the results showed that upon the deposition of Pt, In<sub>2</sub>O<sub>3</sub>-TiO<sub>2</sub> showed an increased electron-scavenging rate constant as well as an enhanced photocatalytic efficiency [25]. These findings demonstrated that charge carrier dynamics could provide further insights into the factors dictating the overall carrier utilization efficiency, which is imperative to design the optimal semiconductor nanoheterostructures for various photoconversion applications. However, there are very few studies in the literature regarding the charge carrier dynamics of three-component Z-scheme system, and their correlation with the resultant photoconversion efficiency is rarely reported. Therefore, a quantitative study on this topic is essential to both the basic understanding and the practical realization of Z-scheme mechanism.

In this work, we presented the interfacial charge dynamics of Z-scheme nanoheterostructures by using Na<sub>x</sub>H<sub>2-x</sub>Ti<sub>3</sub>O<sub>7</sub>-Au-Cu<sub>2</sub>O as the model system. The samples were prepared by selectively depositing a thin layer of Cu<sub>2</sub>O on the Au surface of Au nanoparticle-decorated Na<sub>x</sub>H<sub>2-x</sub>Ti<sub>3</sub>O<sub>7</sub> nanobelts (denoted as ST-Au NBs). For ST-Au NBs, the surface-decorated Au can serve as an effective electron acceptor for ST NBs due to its lower Fermi level (+0.50 V vs. NHE) [26] than the conduction band potential of ST (-0.30 V vs. NHE) [27]. As a consequence, the photoexcited electrons of ST NBs would preferentially transfer to Au nanoparticles, leaving photo-generated holes at ST NBs to achieve charge separation. Because of the electron-charged feature of Au under light illumination, Cu<sub>2</sub>O can be further deposited on the Au surface of ST-Au NBs using a delicate photodeposition method, which resulted in the formation of three-component ST-Au-Cu<sub>2</sub>O Z-scheme NBs. With the introduction of Cu<sub>2</sub>O on the Au surface of ST-Au NBs, the scavenged electrons at Au can transfer to the valence band of Cu<sub>2</sub>O and recombine with the photogenerated holes of Cu<sub>2</sub>O (+0.67 V vs. NHE) [28]. This vectorial charge transfer would give rise to electron accumulation at the conduction band of Cu<sub>2</sub>O and hole concentration at the valence band of ST. The accumulated electrons at Cu<sub>2</sub>O possessed high reduction activity because of the relatively high potential (-1.50 V vs. NHE), while the concentrated holes at ST showed high oxidation power due to the substantially low potential (+3.30 V vs. NHE). Time-resolved PL measurements were conducted to explore the interfacial charge dynamics for the as-prepared ST-Au-Cu<sub>2</sub>O NBs. By probing the emission lifetime of an indicator dye, the electron transfer event between ST and Au for ST-Au NBs and its dependence on the Cu<sub>2</sub>O deposition were quantitatively analyzed. As a result of the significant quantum effect of the deposited Cu<sub>2</sub>O, ST-Au-Cu<sub>2</sub>O NBs with various Cu<sub>2</sub>O thicknesses exhibited tunable relative band offsets, which was exploited to adjust the driving force of electron transfer and therefore modulate the interfacial charge dynamics. The charge carrier transfer in ST-Au-Cu<sub>2</sub>O NBs was further characterized with a photocatalytic process. The results showed that ST-Au-Cu<sub>2</sub>O NBs surpassed pristine ST NBs, and two-component ST-Au NBs and ST-Cu<sub>2</sub>O NBs in photocatalytic activity, presumably due to the more pronounced charge separation property of ST-Au-Cu<sub>2</sub>O Z-scheme system.

## 2. Experimental

### 2.1. Chemicals

All chemicals were of analytical grade and used without further purification.

### 2.2. Preparation of ST NBs and ST-Au NBs

The detailed synthetic approach and relevant characterizations of ST NBs and ST-Au NBs can be found in our previous work [27]. Briefly, Degussa P-25 TiO<sub>2</sub> powder (1.0 g), absolute ethanol (10 mL), and NaOH aqueous solution (10 mL, 10 M) were mixed and allowed for hydrothermal reaction at 200 °C for 24 h. The resultant white slurry was collected by suction filtration and washed with deionized water until the pH of washing solution reached 7.0. The product (ST NBs) was then dried at 60 °C in air for later use. To decorate NBs with Au nanoparticles, ST NBs of 6.0 mg were first dispersed in the reaction solution containing 60 mL deionized water and 30 mL ethanol, followed by the addition of 600 μL NaOH solution (0.1 M). After heated to 50 °C, 60 μL of HAuCl<sub>4</sub> solution (5 mM) was added and the reaction solution was kept at 50 °C for 3 h. The product (ST-Au NBs, with the Au content of 1.0 wt%) was centrifuged, washed with deionized water and ethanol, and then dried at 60 °C in air for later use.

### 2.3. Preparation of ST-Au-Cu<sub>2</sub>O NBs

To deposit Cu<sub>2</sub>O on the Au surface of ST-Au NBs, 5.0 mg of ST-Au NBs were first dispersed in 10 mL ethanol, followed by the addition of 100 μL NaOH aqueous solution (0.1 M) and 150 μL Cu<sup>2+</sup>-citrate solution. Cu<sup>2+</sup>-citrate solution was prepared by mixing 5 mM CuCl<sub>2</sub> and 25 mM sodium citrate in deionized water. The mixed solution was stirred for 30 min in the dark, and then irradiated by a xenon lamp (500 W, with a light intensity of 100 mW/cm<sup>2</sup>) at room temperature for 24 h. The product (ST-Au-Cu<sub>2</sub>O NBs) was centrifuged, washed with deionized water and ethanol, and then dried at 60 °C in air for later use. In this work, various volumes of Cu<sup>2+</sup>-citrate solution (150, 100, 50 μL) were employed to produce ST-Au-Cu<sub>2</sub>O NBs with different Cu<sub>2</sub>O thicknesses. The thus-obtained products were respectively denoted as ST-Au-Cu<sub>2</sub>O.150, ST-Au-Cu<sub>2</sub>O.100 and ST-Au-Cu<sub>2</sub>O.50 NBs. For comparison purpose, two-component Cu<sub>2</sub>O-decorated ST (ST-Cu<sub>2</sub>O) NBs were also prepared by reacting pristine ST NBs with Cu<sup>2+</sup>-citrate solution (50 μL) in the photodeposition process.

### 2.4. Site-selective photodeposition of Pd and PbO<sub>2</sub>

The photodeposition of Pd and PbO<sub>2</sub> on the selective sites of ST-Au-Cu<sub>2</sub>O NBs was carried out according to the previous report with slight modifications [29,30]. To deposit Pd on the Cu<sub>2</sub>O surface, 5 mg of ST-Au-Cu<sub>2</sub>O.50 NBs was dispersed in 10 mL deionized water, followed by the addition of a calculated amount of H<sub>2</sub>PdCl<sub>4</sub> (32 μL, 0.037 M) in the dark. The reaction solution was then irradiated by a xenon lamp (500 W, with a light intensity of 100 mW/cm<sup>2</sup>) at room temperature for 5 h. For the deposition of PbO<sub>2</sub> on the ST surface, Pb(NO<sub>3</sub>)<sub>2</sub> (400 μL, 0.01 M) was used as the Pb source and the same procedure mentioned above was applied except that O<sub>2</sub> acting as electron acceptor was bubbled through the reaction solution.

### 2.5. Preparation of N-doped TiO<sub>2</sub>

N-doped TiO<sub>2</sub> was prepared by annealing P-25 TiO<sub>2</sub> powder in a mixed atmosphere of Ar (200 sccm) and NH<sub>3</sub> (10 sccm) at 500 °C for 2 h [20]. The x value of the product (TiO<sub>2-x</sub>N<sub>x</sub>) was estimated from

**Table 1**

Fitting results for emission decay profiles of C343 in the presence of different samples.

Entry I	A <sub>1</sub>	τ <sub>1</sub> (ns)	A <sub>2</sub>	τ <sub>2</sub> (ns)	<τ> (ns)	χ <sup>2</sup>	k <sub>et</sub> (s <sup>-1</sup> )
C343	9910	3.77	1331	1.55	3.65	2.03	–
C343/ST	8995	3.60	1520	1.51	3.46	2.07	0.15 × 10 <sup>8</sup> (C343 → ST) <sup>a</sup>
C343/Au	9690	3.77	1390	1.54	3.64	2.15	0.008 × 10 <sup>8</sup> (C343 → Au) <sup>a</sup>
C343/Cu <sub>2</sub> O	9800	3.71	846	1.50	3.64	2.02	0.008 × 10 <sup>8</sup> (C343 → Cu <sub>2</sub> O) <sup>a</sup>
C343/ST-Au	4260	3.50	5093	1.47	2.82	2.20	0.65 × 10 <sup>8</sup> (ST → Au) <sup>b</sup>
C343/ST-Au-Cu <sub>2</sub> O <sub>150</sub>	4091	3.29	5273	1.41	2.62	2.25	0.26 × 10 <sup>8</sup> (Au → Cu <sub>2</sub> O <sub>150</sub> ) <sup>c</sup>
Entry II	A <sub>1</sub>	τ <sub>1</sub> (ns)	A <sub>2</sub>	τ <sub>2</sub> (ns)	<τ> (ns)	χ <sup>2</sup>	k <sub>es</sub> (s <sup>-1</sup> )
C343/ST-Au-Cu <sub>2</sub> O <sub>150</sub>	4091	3.29	5273	1.41	2.62	2.25	0.91 × 10 <sup>8</sup> (ST → Au-Cu <sub>2</sub> O <sub>150</sub> ) <sup>d</sup>
C343/ST-Au-Cu <sub>2</sub> O <sub>100</sub>	3450	3.00	7260	1.35	2.24	2.20	1.56 × 10 <sup>8</sup> (ST → Au-Cu <sub>2</sub> O <sub>100</sub> ) <sup>d</sup>
C343/ST-Au-Cu <sub>2</sub> O <sub>50</sub>	2139	2.58	8137	1.33	1.75	2.20	2.81 × 10 <sup>8</sup> (ST → Au-Cu <sub>2</sub> O <sub>50</sub> ) <sup>d</sup>

<sup>a</sup> The value was calculated by the expression  $k_{et}(C343 \rightarrow A) = (1/\langle \tau \rangle)(C343/A) - (1/\langle \tau \rangle)(C343)$ , where A = ST, Au, or Cu<sub>2</sub>O.<sup>b</sup> The value was calculated by the expression  $k_{et}(ST \rightarrow Au) = (1/\langle \tau \rangle)(C343/ST-Au) - (1/\langle \tau \rangle)(C343/ST) - k_{et}(C343 \rightarrow Au)$ .<sup>c</sup> The value was calculated by the expression  $k_{et}(Au \rightarrow Cu_2O) = (1/\langle \tau \rangle)(C343/ST-Au-Cu_2O) - (1/\langle \tau \rangle)(C343/ST-Au) - k_{et}(C343 \rightarrow Cu_2O)$ .<sup>d</sup> The value was calculated by the expression  $k_{es}(A \rightarrow B-C) = (1/\langle \tau \rangle)(C343/A-B-C) - (1/\langle \tau \rangle)(C343/A) - k_{et}(C343 \rightarrow B) - k_{et}(C343 \rightarrow C)$ , where A = ST, B = Au, and C = Cu<sub>2</sub>O<sub>150</sub>, Cu<sub>2</sub>O<sub>100</sub> or Cu<sub>2</sub>O<sub>50</sub>.

X-ray photoelectron spectra (XPS) measurement, approximately 0.28.

## 2.6. PL lifetime measurement

Time-resolved PL spectra were measured using a home-built single photon counting system. GaN diode laser ( $\lambda = 375$  nm) with the pulse duration of 50 ps was used as the excitation source. The signals collected at the excitonic emission of C343 ( $\lambda_{em} = 482$  nm) were dispersed with a grating spectrometer, detected by a high-speed photomultiplier tube, and then correlated using a single photon counting card. Here, C343 ( $1.0 \times 10^{-7}$  M) was used as an indicator dye to monitor the interfacial charge dynamics of ST-Au-Cu<sub>2</sub>O NBs. Upon laser excitation, the photoexcited electrons of C343 were injected into ST NBs due to the higher LUMO potential of C343 ( $-1.23$  V vs. NHE) [31] than the conduction band potential of ST NB, which led to a significant quenching on the PL of C343. By comparing the emission decay profile between C343 and ST NBs-containing C343 (denoted as C343/ST), the electron transfer from C343 to ST NBs can be quantitatively determined. Further spectral comparison among C343/ST, C343/Au, C343/ST-Au samples may reveal the electron transfer event between ST and Au for ST-Au NBs. The emission decay data were analyzed and fitted with a biexponential model which generates two lifetime values,  $\tau_1$  and  $\tau_2$ , and the corresponding amplitudes,  $A_1$  and  $A_2$ . The intensity-average lifetime,  $\langle \tau \rangle$ , was then determined to make an overall comparison. All the fitting results were summarized in Table 1.

## 2.7. Photocatalytic activity measurement

The photocatalytic performance of ST-Au-Cu<sub>2</sub>O NBs was evaluated by monitoring the photodegradation of MB under visible light illumination (500 W xenon lamp, with a bandpass filter of 400–700 nm bandwidth). A quartz tube with a capacity of 20 mL was used as the photoreactor vessel. The photodegradation of MB in the presence of five types of photocatalysts, which included N-doped P-25 TiO<sub>2</sub>, pristine ST NBs, ST-Au NBs, ST-Cu<sub>2</sub>O NBs and ST-Au-Cu<sub>2</sub>O NBs, was evaluated. A typical experiment involved adding 5.0 mg of photocatalyst to 20 mL of MB aqueous solution ( $2.0 \times 10^{-5}$  M) in the photoreactor vessel. Prior to irradiation, the suspension was stirred in the dark for 10 min to reach the adsorption equilibrium of MB with photocatalysts. At various time intervals throughout the irradiation, 1 mL aliquots of reaction solution were withdrawn and centrifuged to remove the photocatalyst. The UV–visible absorption spectrum of the filtrate was then acquired to measure the concentration variation of MB by recording the corresponding absorbance of the maximum intensity peak.

## 2.8. Characterizations

The morphology and dimensions of the samples were examined by a high-resolution transmission electron microscope (TEM, JEOL JEM-3000). The energy dispersive spectrometer (EDS) analysis was performed on the accessory of TEM (JEM-3000). X-ray photoelectron spectroscopy (XPS) measurement was conducted on an Ulvac-PHI 1600 using Al K $\alpha$  radiation under high vacuum conditions. For steady-state photoluminescence (PL) spectroscopy, a Hitachi F-4500 equipped with 150 W xenon lamp was used. UV–visible absorption spectra were collected with a Hitachi U-3900H spectrophotometer at room temperature under ambient atmosphere.

## 3. Results and discussion

### 3.1. Structural investigation

ST NBs with a typical width of 30–70 nm were first obtained in the alkaline hydrothermal process. Decoration of ST NBs with Au nanoparticles was then carried out using a chemical reduction method described in the previous work [27]. As shown in Fig. 1(a), the decorated Au had a size of 8–10 nm and was uniformly distributed on the NB surface. Further deposition of Cu<sub>2</sub>O on the Au surface of ST-Au NBs was performed with a delicate photodeposition approach which used Cu<sup>2+</sup>-citrate complex as the copper source. Note that citrate has been employed as a capping reagent for stabilizing Au nanoparticle suspensions [32]. Here, the use of Cu<sup>2+</sup>-citrate may facilitate the approach of Cu<sup>2+</sup> toward Au surface of ST-Au NBs because part of the citrate moieties may bind to the Au surface. This attribute is crucial to the later successful Cu<sub>2</sub>O deposition on the Au surface. In addition, the use of Cu<sup>2+</sup>-citrate can prevent the precipitation of Cu(OH)<sub>2</sub> before Cu<sup>2+</sup> was reduced to Cu<sup>+</sup>, thus promoting the growth of Cu<sub>2</sub>O [33]. For ST-Au NBs, the band offset between ST and Au caused pronounced charge separation in which the photoexcited electrons of ST NBs preferentially transferred to Au. The electron-charged feature of Au for ST-Au NBs upon light irradiation can be utilized to deposit Cu<sub>2</sub>O on the Au surface. When Cu<sup>2+</sup>-citrate was introduced in alkaline solution under light illumination, Cu<sup>2+</sup> could be reduced to Cu<sup>+</sup> and form the intermediate Cu(OH) which was further dehydrated to produce Cu<sub>2</sub>O [34]. Because the electron-charged Au surface of ST-Au NBs may provide active sites for Cu<sup>2+</sup>-citrate binding and the subsequent Cu<sup>2+</sup> reduction, the formation of Cu<sub>2</sub>O could mostly occur at the Au surface of ST-Au NBs. Therefore, an exclusive deposition of Cu<sub>2</sub>O on the Au surface of ST-Au NBs can be achieved, resulting in the formation of ST-Au-Cu<sub>2</sub>O Z-scheme nanoheterostructures. Fig. 1(b)



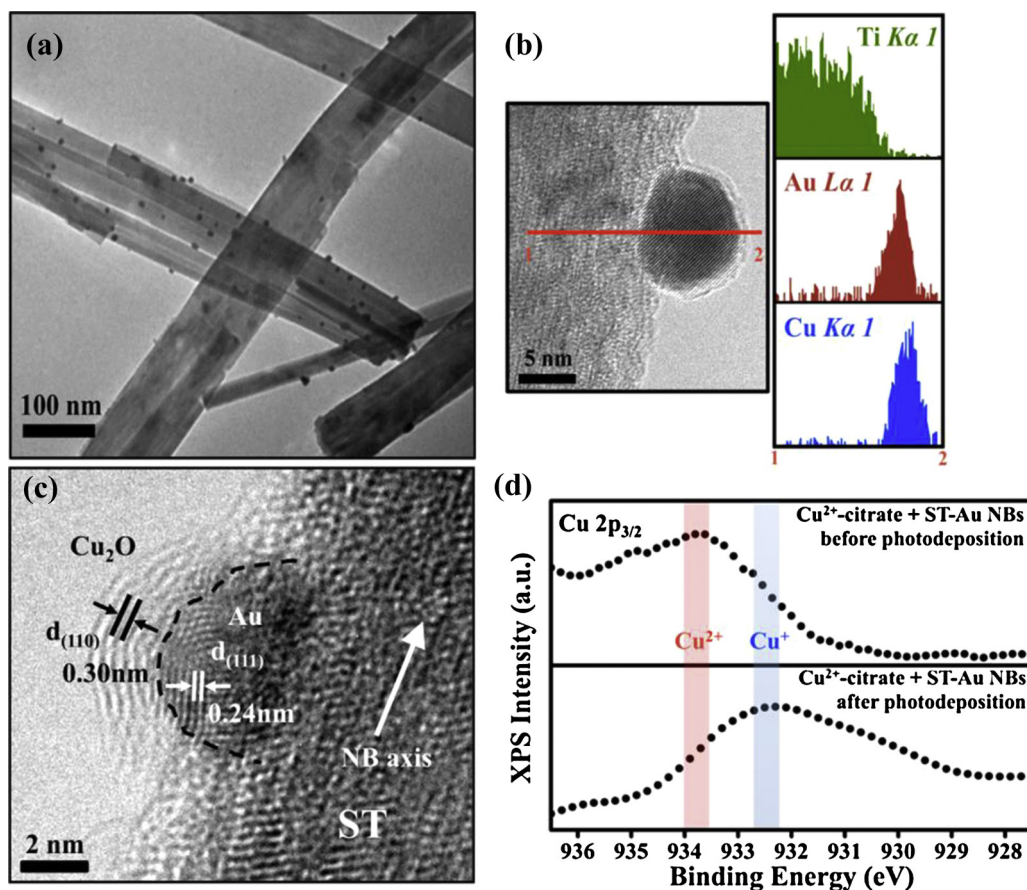


**Fig. 1.** (a) TEM image for ST-Au NBs, (b) TEM-EDS analysis and (c) HRTEM image for ST-Au-Cu<sub>2</sub>O NBs. In (c), the interface between Cu<sub>2</sub>O and Au was highlighted by a dashed line. (d) Cu 2p XPS spectra for Cu<sup>2+</sup>-citrate solution containing ST-Au NBs before and after the photodeposition process.

shows the TEM image of ST-Au NBs after they were reacted with Cu<sup>2+</sup>-citrate in the photodeposition process. Evidently, a hemispherical layer with considerably tiny thickness was deposited on Au surface only. The chemical composition of the deposited layer was further characterized with EDS, High-resolution TEM (HRTEM) and XPS measurements. The TEM-EDS analysis showed that the deposited layer was composed of Cu and O. In Fig. 1(c), the HRTEM image taken at the Au surface clearly revealed two distinct sets of lattice fringes, which can be respectively assigned to fcc Au and cubic Cu<sub>2</sub>O [35]. Moreover, XPS characterization of Fig. 1(d) suggested the prevalence of Cu<sup>+</sup> composition, which as ascribed to the formation of Cu<sub>2</sub>O in the product. Note that the difference in binding energy between Cu<sup>+</sup> (932.5 eV) and Cu<sup>2+</sup> (933.8 eV) was sufficiently large to determine the copper valence of the sample [36–38]. This result, together with the findings from TEM, TEM-EDS and HRTEM, confirmed the successful deposition of Cu<sub>2</sub>O on the Au surface of ST-Au NBs by using Cu<sup>2+</sup>-citrate as the copper source in the photodeposition process. The exact structural feature that Cu<sub>2</sub>O was selectively deposited on the Au surface of ST-Au was vital for realizing the Z-scheme charge transfer mechanism.

### 3.2. Control of Cu<sub>2</sub>O thickness

The thickness of Cu<sub>2</sub>O layer deposited on the Au surface of ST-Au NBs can be further controlled by adjusting the amount of Cu<sup>2+</sup>-citrate used. Fig. 2 displays the gradual decrease in the thickness of the deposited Cu<sub>2</sub>O for ST-Au-Cu<sub>2</sub>O NBs, which was achieved by employing Cu<sup>2+</sup>-citrate solution of decreasing volumes. The grown Cu<sub>2</sub>O had a uniform thickness and fully covered the whole Au surface. From the TEM observations, the average thickness of the

deposited Cu<sub>2</sub>O layer was determined to be  $1.4 \pm 0.1$ ,  $1.2 \pm 0.1$  and  $1.1 \pm 0.1$  nm for the samples prepared with Cu<sup>2+</sup>-citrate solution of 150, 100 and 50  $\mu$ L, respectively. Note that under this thickness range, quantum confinement effect was significant in the deposited Cu<sub>2</sub>O, which can be exploited to tune the band structure of Cu<sub>2</sub>O and therefore modulate the charge carrier dynamics of ST-Au-Cu<sub>2</sub>O NBs. Here we aimed to comprehend the interfacial charge dynamics of Z-scheme ST-Au-Cu<sub>2</sub>O system and study their dependence on the band structure of Cu<sub>2</sub>O by controlling the Cu<sub>2</sub>O thickness.

### 3.3. Charge carrier dynamics of ST-Au-Cu<sub>2</sub>O NBs

To confirm the Z-scheme charge transfer mechanism for the present ST-Au-Cu<sub>2</sub>O NBs, site-selective photodeposition experiments were conducted [29,30]. Under light illumination, the ST body of ST-Au-Cu<sub>2</sub>O NBs was enriched with photogenerated holes while the Cu<sub>2</sub>O layer was charged by photoexcited electrons. The electrons accumulated at Cu<sub>2</sub>O were readily available for the reduction reaction, which can be examined by carrying out the photoreduction of Pd<sup>2+</sup> ions. As revealed in Fig. 3(a)–(c), Pd particles were mostly deposited on the Cu<sub>2</sub>O surface instead of the NB surface. This observation manifested that Pd<sup>2+</sup> ions could be selectively reduced on the Cu<sub>2</sub>O surface of ST-Au-Cu<sub>2</sub>O NBs as a result of the Z-scheme charge transfer. On the other hand, the holes concentrated at ST NBs were highly oxidative and could participate in the photooxidation of Pb<sup>2+</sup>. As Fig. 3(d)–(f) shows, PbO<sub>2</sub> particles were solely grown on the ST NB surface upon the photooxidation of Pb<sup>2+</sup>, which also validated the vectorial charge transfer for ST-Au-Cu<sub>2</sub>O NBs. The demonstrations from the site-selective photodeposition experiments not only provided solid evidence for the Z-scheme

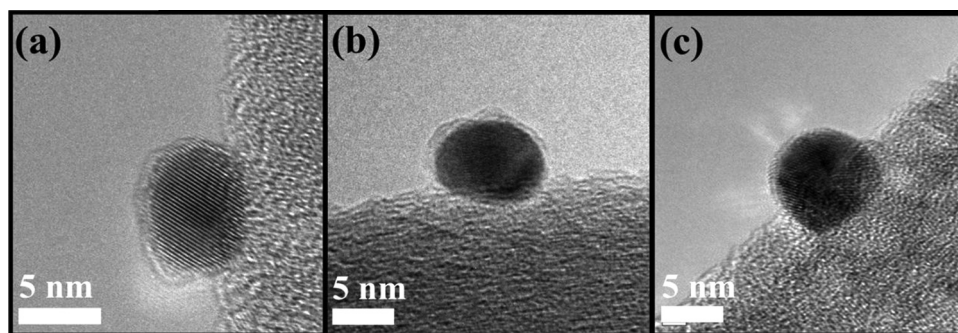


**Fig. 2.** TEM images of ST-Au-Cu<sub>2</sub>O NBs prepared with different volumes of Cu<sup>2+</sup>-citrate: (a) 150 μL, (b) 100 μL and (c) 50 μL.

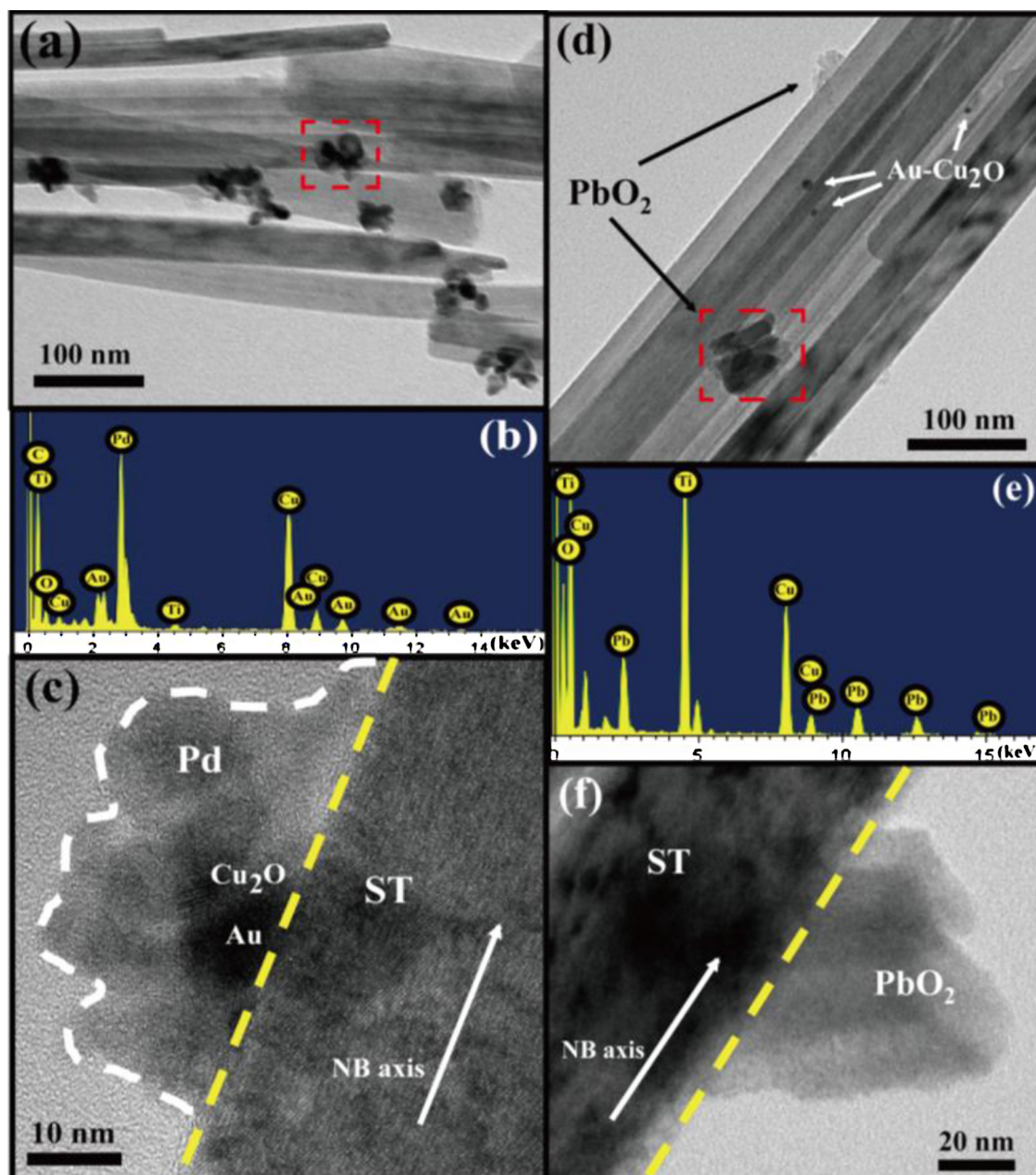


**Fig. 3.** (a) Typical TEM image, (b) TEM-EDS analysis, (c) TEM image taken at the interface region for ST-Au-Cu<sub>2</sub>O NBs upon the photoreduction of Pb<sup>2+</sup>. (d)–(f) shows the results for ST-Au-Cu<sub>2</sub>O NBs upon the photooxidation of Pd<sup>2+</sup>. The EDS spectra of (b) and (e) were respectively taken on the marked regions of (a) and (d).



mechanism but also ruled out the prevalence of other undesirable charge transfer pathways, such as the electron back transfer from the thin  $\text{Cu}_2\text{O}$  layer to Au.

In this work, an indicator dye of Coumarin 343 (denoted as C343) was used to explore the charge carrier dynamics for the NB products. With the carboxylate functional group which shows high affinity to Ti-O bonds, C343 has been widely used as a photosensitizer to inject photoexcited electrons into the conduction band of  $\text{TiO}_2$  for dye-sensitized solar cell applications [31,39]. Here, we employed C343 as a probe molecule to characterize the interfacial charge dynamics of ST NBs. Specifically, the variation of PL intensity and PL lifetime at 482 nm may give insightful information about the fate of charge carriers following light irradiation. Fig. 4(a) shows the steady-state PL spectra of C343 under different experimental conditions. When pristine ST NBs of a given amount were dispersed in C343 (sample was denoted as C343/ST), the PL intensity of C343 was decayed. The PL decay of C343 became more significant as a commensurate amount of ST-Au NBs or ST-Au- $\text{Cu}_2\text{O}$  NBs was introduced (sample was respectively denoted as C343/ST-Au or C343/ST-Au- $\text{Cu}_2\text{O}$ ). Note that for C343/ST, C343/ST-Au and C343/ST-Au- $\text{Cu}_2\text{O}$ , photocatalysis did not occur to decompose C343 during the short time period of PL measurement. The as-observed PL decay of C343 in C343/ST, C343/ST-Au and C343/ST-Au- $\text{Cu}_2\text{O}$  samples was thus mainly attributed to the occurrence of charge separation upon light irradiation. Because ST has a lower conduction potential ( $-0.30\text{ V}$  vs. NHE) than the lowest-unoccupied molecular orbital (LUMO) potential of C343 ( $-1.23\text{ V}$  vs. NHE), the photoexcited electrons of C343 would preferentially transfer to ST, leading to the depletion of free electrons for C343 and the subsequent decay of its PL. When Au was present on ST NBs, the photoexcited electrons of C343 may further transfer to Au through the ST/Au interface since Au has much lower Fermi level ( $+0.50\text{ V}$  vs. NHE). This phenomenon caused a higher extent of free electron depletion for C343, which was responsible for the more significant PL decay of C343 observed for C343/ST-Au. Similar interpretation may apply to C343/ST-Au- $\text{Cu}_2\text{O}$  sample in which a much more pronounced decay of PL intensity was noticed and can be regarded as a result of the further electron transfer from the Fermi level of Au to the valence band of  $\text{Cu}_2\text{O}$ . It should be mentioned that the electronic interaction of C343 with pure Au or pure  $\text{Cu}_2\text{O}$  was insignificant because the PL of C343 was not decayed in the presence of Au or  $\text{Cu}_2\text{O}$  (data not shown here). This outcome supports the contention that the more significant PL decay of C343 for C343/ST-Au and C343/ST-Au- $\text{Cu}_2\text{O}$  mainly resulted from the further electron transfer from ST to Au and then to  $\text{Cu}_2\text{O}$ .

To further elucidate the electron transfer event within the samples, time-resolved PL measurements were conducted. Fig. 4(b) compares the time-resolved PL spectra of C343 for four relevant samples. The emission decay profiles of C343 for the four samples all exhibited a biexponential model in which two decay components were derived. The intensity-average lifetime was calculated to make an overall comparison of the emission decay behavior. For pure C343, an emission lifetime of  $3.65\text{ ns}$  was recorded, fairly close to the reported value of around  $3.4\text{--}4.0\text{ ns}$  [31,40,41]. As to the C343/ST sample, a shortened emission lifetime of  $3.46\text{ ns}$  was observed, indicating the emergence of a nonradiative pathway from the electronic interaction between C343 and ST. This suggestion was supported by the PL decay of C343 observed for C343/ST sample. It was assumed that the electron transfer from C343 to ST dictated the emission decay of C343 for C343/ST sample. The electron-transfer rate constant ( $k_{\text{et}}$ ) from C343 to ST can then be calculated by the expression  $k_{\text{et}}(\text{C343} \rightarrow \text{ST}) = (1/\langle\tau\rangle)(\text{C343/ST}) - (1/\langle\tau\rangle)(\text{C343})$  [25], approximately  $0.15 \times 10^8\text{ s}^{-1}$ . Table 1 summarizes the electron-transfer rate constants of different processes calculated from the relevant samples. It should be noted that the emission lifetime of C343 in the

presence of Au or  $\text{Cu}_2\text{O}$  were both  $3.64\text{ ns}$ , giving  $k_{\text{et}}(\text{C343} \rightarrow \text{Au})$  and  $k_{\text{et}}(\text{C343} \rightarrow \text{Cu}_2\text{O})$  as  $0.008 \times 10^8\text{ s}^{-1}$ . This value was about two order of magnitude smaller than that of  $k_{\text{et}}(\text{C343} \rightarrow \text{ST})$ , verifying the relatively insignificant electronic interaction of C343 with Au or  $\text{Cu}_2\text{O}$ . For C343 that contained ST-Au NBs, the average lifetime ( $\langle\tau\rangle = 2.82\text{ ns}$ ) was found shorter than that of C343/ST. Given that the electronic interaction between C343 and Au was relatively minor, we ascribed the C343 emission lifetime shortening of C343/ST-Au to the further electron transfer from ST to Au. By comparing the average lifetime of C343 between C343/ST-Au and C343/ST samples and deducting the contribution of electron transfer from C343 to Au, we obtained  $k_{\text{et}}(\text{ST} \rightarrow \text{Au})$  as  $0.65 \times 10^{-8}\text{ s}^{-1}$ . When  $\text{Cu}_2\text{O}$  was present on the Au surface of ST-Au NBs (ST-Au- $\text{Cu}_2\text{O}$ .150), the shrinkage of C343 emission lifetime became more noticeable, inferring the further electron transfer from Au to  $\text{Cu}_2\text{O}$  through the Au/ $\text{Cu}_2\text{O}$  interface upon light irradiation. By use of an analogous calculation method,  $k_{\text{et}}(\text{Au} \rightarrow \text{Cu}_2\text{O}.150)$  was determined to be  $0.26 \times 10^{-8}\text{ s}^{-1}$ , which was of the same order of magnitude as  $k_{\text{et}}(\text{ST} \rightarrow \text{Au})$ . This result confirms that  $\text{Cu}_2\text{O}$  acted as an effective electron scavenger for ST-Au NBs by accepting the photoexcited electrons from Au as is demonstrated in the Z-scheme mechanism. This vectorial charge transfer led to increasingly pronounced charge separation for ST-Au- $\text{Cu}_2\text{O}$  NBs. To highlight the contribution of  $\text{Cu}_2\text{O}$  to the overall charge separation of NBs, Au and  $\text{Cu}_2\text{O}$  were regarded as an electron scavenger ensemble for ST. Accordingly, the rate constant of electron-scavenging from ST ( $k_{\text{es}}$ ) can be computed, approximately  $0.91 \times 10^8\text{ s}^{-1}$  for ST-Au- $\text{Cu}_2\text{O}$ .150 sample. It should be noted that although the time-resolve PL data were acquired from the indicator dye C343 instead directly from the NBs, the carrier dynamics results from this work still described the charge transfer events across the interface of ST-Au- $\text{Cu}_2\text{O}$ , which may depict the charge transfer scenario for the practical Z-scheme mechanism.

#### 3.4. Quantum size effect of $\text{Cu}_2\text{O}$

In CdS-Au- $\text{TiO}_2$  Z-scheme nanojunction system, the photocatalytic activity of the samples could be enhanced by appropriately reducing the thickness of the deposited CdS [6]. Due to the quantum size effect, the conduction band potential of CdS for CdS-Au- $\text{TiO}_2$  with reduced CdS thickness was raised, giving rise to increasingly strong reducing power to enhance the photocatalytic activity. Similar to the CdS-Au- $\text{TiO}_2$  system, the deposited  $\text{Cu}_2\text{O}$  in the present ST-Au- $\text{Cu}_2\text{O}$  NBs was considerably thin and also exhibited quantum effect, which can be exploited to tune the band structure of  $\text{Cu}_2\text{O}$  and modulate the charge carrier dynamics of the samples. As a result of the varied band offset, an enlarged band energy difference could be attained in ST-Au- $\text{Cu}_2\text{O}$  NBs, which might further increase the rate of electron scavenging from ST. As represented in Fig. 4(c), when the thickness of  $\text{Cu}_2\text{O}$  for ST-Au- $\text{Cu}_2\text{O}$  NBs decreased from  $1.4$  to  $1.2\text{ nm}$ , the emission lifetime of C343 was reduced from  $2.62$  to  $2.24\text{ ns}$ . This phenomenon signifies that the  $1.2\text{ nm}$  thick  $\text{Cu}_2\text{O}$  modulated the interfacial charge transfer of ST-Au NBs more significantly by attracting more electrons from ST, which conducted to the more pronounced charge carrier separation for ST-Au- $\text{Cu}_2\text{O}$ .100 with an electron-scavenging rate constant of  $1.56 \times 10^8\text{ s}^{-1}$ . Further decrease in the thickness of  $\text{Cu}_2\text{O}$  for ST-Au- $\text{Cu}_2\text{O}$  NBs ( $1.1\text{ nm}$ ) caused an even shorter emission lifetime of C343 ( $\langle\tau\rangle = 1.75\text{ ns}$ ), suggesting that charge separation of ST-Au- $\text{Cu}_2\text{O}$  became increasingly conspicuous as  $\text{Cu}_2\text{O}$  of  $1.1\text{ nm}$  thick was deposited. The corresponding electron-scavenging rate constant was estimated to be  $2.81 \times 10^8\text{ s}^{-1}$ . The increase of electron-scavenging rate constant for ST-Au- $\text{Cu}_2\text{O}$  NBs with decreasing  $\text{Cu}_2\text{O}$  thickness can be understood from the more significant quantum size effect of  $\text{Cu}_2\text{O}$  which caused larger driving force of interfacial electron transfer. Note that the Bohr radius of  $\text{Cu}_2\text{O}$  is about  $0.7\text{ nm}$ , signifying that quantum

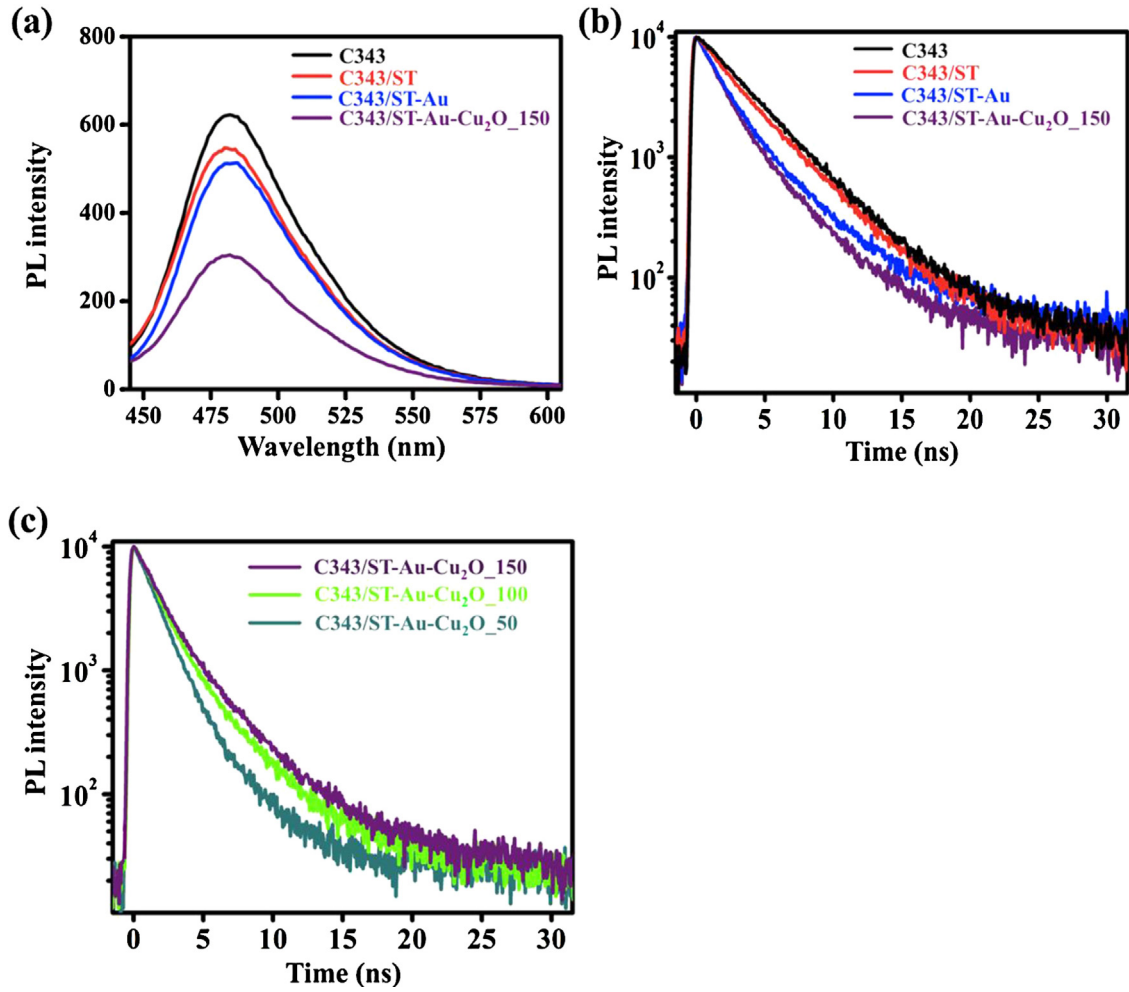


**Fig. 4.** (a) Steady-state PL spectra and (b) time-resolved PL spectra of C343 in the presence of different samples. (c) Comparison of PL decay profile for C343 that contained ST-Au-Cu<sub>2</sub>O NBs with different Cu<sub>2</sub>O thicknesses.

size effect becomes noticeable once the characteristic size of Cu<sub>2</sub>O is smaller than 1.4 nm [42,43]. The average thickness of Cu<sub>2</sub>O for the three ST-Au-Cu<sub>2</sub>O NBs was essentially small, suggesting the prevalence of pronounced quantum size effect. The bandgap expansion for the deposited Cu<sub>2</sub>O resulting from the size effect could be estimated by the Brus equation [43,44]:

$$E_g^* = E_g^{\text{bulk}} + \frac{\hbar^2 \pi^2}{2\mu L^2} - \frac{1.8e^2}{\epsilon L} - \frac{0.124e^4 \mu}{\hbar^2 \epsilon^2 n^2} \quad (1)$$

In (1),  $\epsilon$  is the dielectric constant,  $\mu$  is the reduced mass given by  $1/\mu = (1/m_e^* + 1/m_h^*)$  where  $m_e^*$  and  $m_h^*$  are the effective masses of electrons and holes in the bulk Cu<sub>2</sub>O, and  $L$  is the thickness of the deposited Cu<sub>2</sub>O. By using the values of  $m_e^* = 0.99 m_0$ ,  $m_h^* = 0.58 m_0$ ,  $\epsilon = 7.11$  and  $E_g^{\text{bulk}} = 2.17$  eV for Cu<sub>2</sub>O, the bandgap of the deposited Cu<sub>2</sub>O ( $E_g^*$ ) was calculated to be 2.76, 2.90 and 3.05 eV for ST-Au-Cu<sub>2</sub>O\_150, ST-Au-Cu<sub>2</sub>O\_100 and ST-Au-Cu<sub>2</sub>O\_50, respectively. As the bandgap expanded with decreasing size, the energy level of conduction band and valence band respectively shifted toward higher and lower potential. The extent of such potential shifts can be computed using the following empirical expression [45]:

$$\Delta E_{\text{CB}} = \frac{\hbar^2}{8m_e^* L^2} \quad (2)$$

$$\Delta E_{\text{VB}} = \frac{\hbar^2}{8m_h^* L^2} \quad (3)$$

With the results derived from (2) and (3), the band structure of the deposited Cu<sub>2</sub>O in ST-Au-Cu<sub>2</sub>O NBs can be further determined as follows. For ST-Au-Cu<sub>2</sub>O\_150, ST-Au-Cu<sub>2</sub>O\_100 and ST-Au-Cu<sub>2</sub>O\_50, the conduction band potential of Cu<sub>2</sub>O, respectively, shifted to −1.72 V, −1.77 V and −1.82 V vs. NHE, while the valence band potential of Cu<sub>2</sub>O was located at +1.04 V, +1.13 V and +1.23 V vs. NHE. For the present Z-scheme ST-Au-Cu<sub>2</sub>O NBs, the scavenged electrons at Au may further transfer to the valence band of Cu<sub>2</sub>O and recombine with the localized holes. According to Marcus theory [46,47], the energy level between the Fermi level of Au (donor state) and the valence band of Cu<sub>2</sub>O (acceptor state) would determine the driving force for the interfacial electron transfer. This energy difference ( $-\Delta G$ ) [48,49] was 0.53, 0.62 and 0.72 eV for ST-Au-Cu<sub>2</sub>O NBs with the Cu<sub>2</sub>O thickness of 1.4, 1.2 and 1.1 nm, respectively. As the Cu<sub>2</sub>O thickness decreased, the driving force of interfacial electron transfer for ST-Au-Cu<sub>2</sub>O NBs increased, leading to the increasingly conspicuous charge separation and the enhanced electron-scavenging rate constant as observed.

### 3.5. Photocatalytic properties

To further correlate the carrier dynamics results with the photocatalytic efficiency of the samples, photocatalysis experiments were performed by using methylene blue (denoted as MB) as the test pollutant. MB is a typical dye that can be decomposed by reacting with the active oxygen species (e.g.  $\cdot\text{OH}$  and  $\cdot\text{O}_2^-$  radicals)

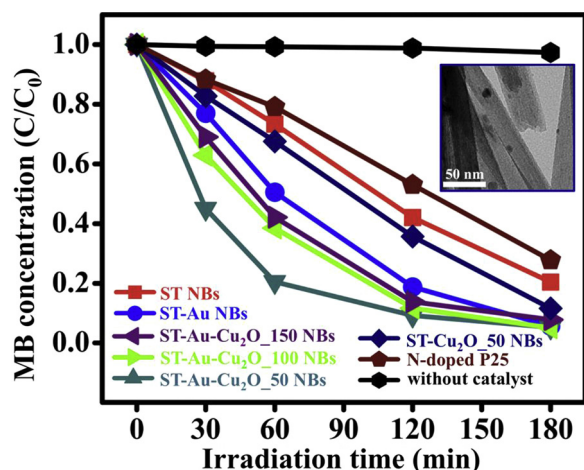


Fig. 5.  $C/C_0$  vs. irradiation time plots for MB photodegradation without any catalyst and in the presence of five kinds of relevant samples. Inset shows the TEM image of ST-Au-Cu<sub>2</sub>O NBs.

following the irradiation on photocatalysts [50–54]. Note that the redox potentials of  $O_2/\cdot O_2^-$  and  $H_2O/\cdot OH$  are  $-0.046$  and  $+2.8$  V vs. NHE, respectively [55]. Since ST-Au-Cu<sub>2</sub>O NBs had sufficiently high reducing ( $-1.50$  V vs. NHE) and oxidizing powers ( $+3.30$  V vs. NHE) under light illumination, both  $\cdot OH$  and  $\cdot O_2^-$  radicals could be generated and participate in the degradation of MB. Five kinds of photocatalysts, including N-doped P-25 TiO<sub>2</sub>, pristine ST NBs, ST-Au NBs, ST-Cu<sub>2</sub>O NBs and ST-Au-Cu<sub>2</sub>O NBs (ST-Au-Cu<sub>2</sub>O-150, ST-Au-Cu<sub>2</sub>O-100, ST-Au-Cu<sub>2</sub>O-50), were used for MB photodegradation under the same experimental conditions. Fig. 5 compares the MB photodegradation results of all the samples under visible light illumination, which revealed several important facts as stated below. First, all the three ST-Au-Cu<sub>2</sub>O NBs performed better toward MB photodegradation than pristine ST NB, ST-Cu<sub>2</sub>O NBs and ST-Au NBs did. Here, ST-Au and ST-Cu<sub>2</sub>O NBs respectively represented the typical metal-semiconductor and semiconductor-semiconductor heterostructure systems [56,57] that have been widely developed for photocatalysis applications. The superiority of ST-Au-Cu<sub>2</sub>O over the two-component counterparts of ST-Au and ST-Cu<sub>2</sub>O illustrated the advantageous feature of Z-scheme mechanism in photocatalytic processes. Second, as compared to the N-doped P-25 TiO<sub>2</sub> powder, the three ST-Au-Cu<sub>2</sub>O NBs all exhibited better photocatalytic performance under visible light illumination. It should be noted that ST NBs can effectively absorb visible light to carry out photocatalytic reactions [27]. The visible absorption of ST NBs derived from the intercalated Na atoms which invoked interband transition within the energy gap of ST to result in the redshift of absorption toward visible region. For ST-Au-Cu<sub>2</sub>O NBs, the recorded visible absorption band was more pronounced (data not shown here), presumably resulting from the effective light absorption of Cu<sub>2</sub>O. Because ST and Cu<sub>2</sub>O were both capable of harvesting visible light, the present ST-Au-Cu<sub>2</sub>O NBs may find promising potentials in efficient solar energy conversion. Third, ST-Au-Cu<sub>2</sub>O NBs showed enhanced photocatalytic efficiency as the Cu<sub>2</sub>O thickness decreased. This outcome was consistent with the results of charge carrier dynamics, in which an increased electron-scavenging rate constant was observed for ST-Au-Cu<sub>2</sub>O NBs with decreasing Cu<sub>2</sub>O thickness. As the Cu<sub>2</sub>O thickness decreased, charge separation became increasingly conspicuous at the ST/Au interface, leaving abundant photoexcited electrons and holes at the conduction band of Cu<sub>2</sub>O and the valence band of ST. The increase in the number of charge carriers further led to the enhancement in the photocatalytic performance. It should be mentioned that the three ST-Au-Cu<sub>2</sub>O samples showed nearly identical MB adsorption

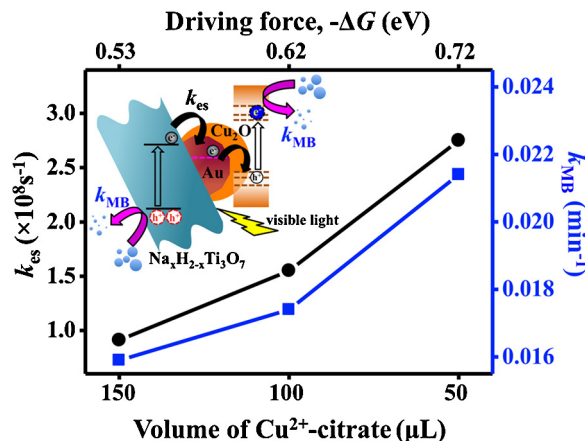


Fig. 6. Correlations of electron-scavenging rate constant ( $k_{es}$ ) and rate constant of MB photodegradation ( $k_{MB}$ ) with the amount of Cu<sup>2+</sup>-citrate and the driving force ( $-\Delta G$ ) of electron transfer for ST-Au-Cu<sub>2</sub>O NBs.

capability. After stirring in the dark for 10 min, 9.6, 9.5 and 9.7% of MB was adsorbed by using ST-Au-Cu<sub>2</sub>O-150, ST-Au-Cu<sub>2</sub>O-100 and ST-Au-Cu<sub>2</sub>O-50, respectively. This demonstration suggests that the origin of the observed enhancement of photocatalytic activity was not related to the structural effect concerning surface area or dye adsorption, but lay in the difference of charge carrier dynamics modulated by the Cu<sub>2</sub>O thickness. To quantitatively compare the photocatalytic performance of the three ST-Au-Cu<sub>2</sub>O NBs, the rate constant of MB photodegradation ( $k_{MB}$ ) was calculated using the pseudo-1st-order approximation, which gave  $k_{MB}$  value of 0.015, 0.017, and 0.021 min<sup>-1</sup> for ST-Au-Cu<sub>2</sub>O-150, ST-Au-Cu<sub>2</sub>O-100 and ST-Au-Cu<sub>2</sub>O-50, respectively. As displayed in Fig. 6, the trend in  $k_{MB}$  variation for ST-Au-Cu<sub>2</sub>O NBs with decreasing Cu<sub>2</sub>O thickness corresponded well with that in  $k_{es}$  change. This correspondence manifests that understanding of charge carrier dynamics is conducive to the realization of Z-scheme mechanism. As a final note, the plasmonic effect [7,58] of Au was suggested to be insignificant in the current system considering that the content of Au of ST-Au-Cu<sub>2</sub>O NBs was as low as 1.0 wt%. With this consideration, the correlation between charge carrier dynamics and photocatalytic efficiency for the present ST-Au-Cu<sub>2</sub>O Z-scheme system can be validated.

#### 4. Conclusions

In conclusion, ST-Au-Cu<sub>2</sub>O NBs were prepared and used as the model system to investigate the interfacial charge dynamics of Z-scheme charge transfer mechanism. With the deposition of Cu<sub>2</sub>O on the Au surface of ST-Au NBs, a vectorial charge transfer from ST, through Au, finally to Cu<sub>2</sub>O was achieved in ST-Au-Cu<sub>2</sub>O, giving rise to superior charge separation property over the two-component counterparts of ST-Au and ST-Cu<sub>2</sub>O. The quantum size effect was significant in the deposited Cu<sub>2</sub>O, which was exploited to tune the band structure of Cu<sub>2</sub>O, modulate the charge carrier dynamics of ST-Au-Cu<sub>2</sub>O NBs, and thereby enhance the resultant photocatalytic performance. The vectorial charge transfer feature as well as the visible absorption capability makes the present ST-Au-Cu<sub>2</sub>O NBs especially promising in practical photocatalytic applications such as overall solar water splitting. The ability to modulate the charge carrier dynamics of Z-scheme nanoheterostructures has significant implications in the development of photocatalyst technology, especially the strategies of materials selection and heterojunction engineering. The development of photocatalyst technology that operates with Z-scheme principle is particularly imperative from the view point of efficient solar energy conversion. By taking into



account the underlying origins of the charge carrier dynamics of ST-Au-Cu<sub>2</sub>O NBs as the guidelines, one may construct an essentially unique yet practically versatile Z-scheme platform capable of realizing artificial photosynthesis.

## Acknowledgements

This work was supported by the Ministry of Science and Technology of the Republic of China (Taiwan) under grants NSC-102-2113-M-009-005-MY2 and NSC-102-3113-P-009-002.

## References

- [1] N.S. Lewis, D.G. Nocera, *PNAS* 103 (2006) 15729–15735.
- [2] B. Conlan, *Photosynth. Res.* 98 (2008) 687–700.
- [3] O. Kruse, J. Rupprecht, J.H. Mussgnug, G.C. Dismukes, B. Hankamer, *Photochem. Photobiol. Sci.* 4 (2005) 957–969.
- [4] A. Kudo, Y. Miseki, *Chem. Soc. Rev.* 38 (2009) 253–278.
- [5] K. Maeda, *ACS Catal.* 3 (2013) 1486–1503.
- [6] H. Tada, T. Mitsui, T. Kiyonaga, T. Akita, K. Tanaka, *Nat. Mater.* 5 (2006) 782–786.
- [7] J. Hou, C. Yang, Z. Wang, Q. Ji, Y. Li, G. Huang, S. Jiao, H. Zhu, *Appl. Catal. B: Environ.* 142–143 (2013) 579–589.
- [8] H.J. Yun, H. Lee, N.D. Kim, D.M. Lee, S. Yu, J. Yi, *ACS Nano* 5 (2011) 4084–4090.
- [9] H. Zhu, B. Yang, J. Xu, Z. Fu, M. Wen, T. Cuo, S. Fu, J. Zuo, S. Zhang, *Appl. Catal. B: Environ.* 90 (2009) 463–469.
- [10] X. Wang, G. Liu, L. Wang, Z.-G. Chen, G.-Q. Lu, H.-M. Cheng, *Adv. Energy Mater.* 2 (2012) 42–46.
- [11] X. Wang, S. Li, Y. Ma, H. Yu, J. Yu, *J. Phys. Chem. C* 115 (2011) 14648–14655.
- [12] A. Iwase, Y.H. Ng, Y. Ishiguro, A. Kudo, R. Amal, *J. Am. Chem. Soc.* 133 (2011) 11054–11057.
- [13] L. Ye, J. Liu, C. Gong, L. Tian, T. Peng, L. Zan, *ACS Catal.* 2 (2012) 1677–1683.
- [14] L. Ding, S. Lou, J. Ding, D. Zhang, H. Zhu, T. Fan, *Int. J. Hydrogen Energy* 38 (2013) 8244–8253.
- [15] H. Yang, S.V. Kershaw, Y. Wang, X. Gong, S. Kalytchuk, A.L. Rogach, W.Y. Teoh, *J. Phys. Chem. C* 117 (2013) 20406–20414.
- [16] Z. Chen, W. Wang, Z. Zhang, X. Fang, *J. Phys. Chem. C* 117 (2013) 19346–19352.
- [17] Z.B. Yu, Y.P. Xie, G. Liu, G.Q. Lu, X.L. Ma, H.-M. Cheng, *J. Mater. Chem. A* 1 (2013) 2773–2776.
- [18] Y. Min, G. He, Q. Xu, Y. Chen, *J. Mater. Chem. A* 2 (2014) 1294–1301.
- [19] C.-T. Yuan, Y.-G. Wang, K.-Y. Huang, T.-Y. Chen, P. Yu, J. Tang, A. Sitt, U. Banin, O. Millo, *ACS Nano* 6 (2012) 176–182.
- [20] P.V. Kamat, *Acc. Chem. Res.* 45 (2012) 1906–1915.
- [21] P.V. Kamat, *J. Phys. Chem. Lett.* 3 (2012) 663–672.
- [22] S. Krishnamurthy, P.V. Kamat, *J. Phys. Chem. C* 117 (2013) 571–577.
- [23] T.-T. Yang, W.-T. Chen, Y.-J. Hsu, K.-H. Wei, T.-Y. Lin, T.-W. Lin, *J. Phys. Chem. C* 114 (2010) 11414–11420.
- [24] Y.-F. Lin, Y.-J. Hsu, *Appl. Catal. B: Environ.* 130–131 (2013) 93–98.
- [25] Y.-C. Chen, Y.-C. Pu, Y.-J. Hsu, *J. Phys. Chem. C* 116 (2012) 2967–2975.
- [26] P.V. Kamat, B. Shanghavi, *J. Phys. Chem. B* 101 (1997) 7675–7679.
- [27] Y.-C. Pu, Y.-C. Chen, Y.-J. Hsu, *Appl. Catal. B: Environ.* 97 (2010) 389–397.
- [28] Y. Bessekhouad, D. Robert, J.-V. Weber, *Catal. Today* 101 (2005) 315–321.
- [29] A.A. Ismail, D.W. Bahnemann, S.A. Al-Sayari, *Appl. Catal. A: Gen.* 431–432 (2012) 62–68.
- [30] R. Li, F. Zhang, D. Wang, J. Yang, M. Li, J. Zhu, X. Zhou, H. Han, C. Li, *Nat. Commun.* 4 (2013) 1432.
- [31] K. Hara, T. Sato, R. Katoh, A. Furube, Y. Ohga, A. Shinpo, S. Suga, K. Sayama, H. Sugihara, H. Arakawa, *J. Phys. Chem. B* 107 (2003) 597–606.
- [32] S. Biggs, P. Mulvaney, C.F. Zukoski, F. Grieser, *J. Am. Chem. Soc.* 116 (1994) 9150–9157.
- [33] I.-C. Chang, P.-C. Chen, M.-C. Tsai, T.-T. Chen, M.-H. Yang, H.-T. Chiu, C.-Y. Lee, *CrystEngComm* 15 (2013) 2363–2366.
- [34] S.-J. Chen, X.-T. Chen, Z. Xue, L.-H. Li, X.-Z. You, *J. Cryst. Growth* 246 (2002) 169–175.
- [35] For bulk fcc Au,  $d(1\ 1\ 1) = 0.2355\text{ nm}$  from JCPDS 04-0784. For bulk cubic Cu<sub>2</sub>O,  $d(1\ 1\ 0) = 0.30200\text{ nm}$  from JCPDS-05-0667.
- [36] T.L. Freeman, S.D. Evans, *Thin Solid Films* 244 (1994) 784–788.
- [37] S.H.Y. Lo, Y.-Y. Wang, C. Chao, *J. Colloid Interface Sci.* 310 (2007) 190–195.
- [38] M.S. El-Deab, *Mater. Chem. Phys.* 129 (2011) 223–227.
- [39] F. Odobel, L. Pleux, Y. Pellegrin, E. Blart, *Acc. Chem. Res.* 43 (2010) 1063–1071.
- [40] K. Murakoshi, S. Yanagida, M. Capel, E.W. Castner, Jr., *Interfacial electron Transfer Dynamics of Photosensitized Zinc Oxide Nanoclusters*. ACS Symp. Ser. Washington DC 679, 1997, p 221.
- [41] S. Ghosh, A.K. Mandal, A.K. Das, T. Mondal, K. Bhattacharyya, *Phys. Chem. Chem. Phys.* 14 (2012) 9749–9757.
- [42] P. Pouloupoulos, S. Baskoutas, S.D. Pappas, C.S. Garoufalidis, S.A. Droulias, A. Zamani, V. Kapaklis, *J. Phys. Chem. C* 115 (2011) 14839–14843.
- [43] K. Borgohain, N. Murase, S. Mahamuni, *J. Appl. Phys.* 92 (2002) 1292–1297.
- [44] G. Dresselhaus, *J. Phys. Chem. Solids* 1 (1956) 15–23.
- [45] A.L. Stroyuk, A.I. Kryukov, S. Ya Kuchmii, V.D. Pokhodenko, *Theor. Exp. Chem.* 41 (2005) 207–228.
- [46] R.A. Marcus, *J. Chem. Phys.* 43 (1965) 679–701.
- [47] Y.Q. Gao, R.A. Marcus, *J. Chem. Phys.* 113 (2000) 6351–6360.
- [48] I. Robel, M. Kuno, P.V. Kamat, *J. Am. Chem. Soc.* 129 (2007) 4136–4137.
- [49] V. Chakrapani, K. Tvrdy, P.V. Kamat, *J. Am. Chem. Soc.* 132 (2010) 1228–1229.
- [50] C.-H. Wu, J.-M. Chern, *Ind. Eng. Chem. Res.* 45 (2006) 6450–6457.
- [51] S. Lakshmi, R. Renganathan, S. Fujita, *J. Photochem. Photobiol. A: Chem.* 88 (1995) 163–167.
- [52] N. Talebian, M.R. Niforoushan, *Thin Solid Films* 518 (2010) 2210–2215.
- [53] A.D. Mani, B.R. Raju, N. Xanthopoulos, P. Ghosal, B. Sreedhar, C. Subrahmanyam, *Chem. Eng. J.* 228 (2013) 545–553.
- [54] D. Zhao, G. Sheng, C. Chen, X. Wang, *Appl. Catal. B: Environ.* 111–112 (2012) 303–308.
- [55] M. Miyauchi, Y. Nukui, D. Atarashi, E. Sakai, *ACS Appl. Mater. Interf.* 5 (2013) 9770–9776.
- [56] N. Zhang, S. Liu, Y.-J. Xu, *Nanoscale* 4 (2012) 2227–2238.
- [57] Y. Wang, Q. Wang, X. Zhan, F. Wang, M. Safdar, J. He, *Nanoscale* 5 (2013) 8326–8339.
- [58] J. Hou, Z. Wang, C. Yang, W. Zhou, S. Jiao, H. Zhu, *J. Phys. Chem. C* 117 (2013) 5132–5141.